**Biophysical Journal, Volume *118***

## Supplemental Information

# Molecular Mechanism for Attractant Signaling to DHMA by *E. coli* Tsr

**Asuka A. Orr, Jingyun Yang, Nitesh Sule, Ravi Chawla, Kenneth G. Hull, Mingzhao Zhu, Daniel Romo, Pushkar P. Lele, Arul Jayaraman, Michael D. Manson, and Phanourios Tamamis**

# Molecular Mechanism for Attractant Signaling to DHMA by *E. coli* Tsr

## Supporting Material

Asuka A. Orr[1], Jingyun Yang[1], Nitesh Sule[1], Ravi Chawla[1], Kenneth G. Hull[2], Mingzhao Zhu[2], Daniel Romo[2], Pushkar P. Lele[1], Arul Jayaraman[1], Michael D. Manson[3*], Phanourios Tamamis[1*]

[1]Artie McFerrin Department of Chemical Engineering, Texas A&M University, College Station, TX 77843, USA

[2]Department of Chemistry & Biochemistry and CPRIT Synthesis and Drug-Lead Discovery Laboratory, Baylor University, Waco, TX 76798, USA

[3]Department of Biology, Texas A&M University, College Station, TX 77843, USA

[*]Correspondence: mike@bio.tamu.edu, tamamis@tamu.edu

Tel.: +1-979-862-1610

Fax: +1-979-845-6446

**Supporting computational methods**

**Docking (*S*)-DHMA to pTsr.** We performed a nearly exhaustive search of all binding modes of (*S*)-DHMA in complex with *E. coli* Tsr, which aimed to predict the most energetically favorable binding mode through an in-house developed docking-refinement protocol (1-6) for use as the initial structure for subsequent MD simulations and detailed analysis. The protocol can be divided into the following stages: (1) the initial positioning of the ligand within the receptor binding pocket, based on available experimental data; (2) multiple short MD docking simulations nearly exhaustively searching binding conformations of the ligand within the receptor binding pocket, with the ligand constrained to the binding pocket though harmonic and quartic spherical potentials and the binding pocket of the receptor unconstrained; (3) interaction energy calculations evaluating the resulting binding conformations to select the most probable binding modes generated by the short docking simulations; and (4) explicit-solvent MD simulations and physical-chemistry based free-energy calculations are employed to identify the most favorable binding mode of the ligand:receptor complex (Figure S1). The docking-refinement protocol was first developed and executed to study and compare the binding of agonist and antagonist compounds to the mouse aryl hydrocarbon receptor (2). Since its debut, we have applied the docking-refinement protocol to detect the most energetically favorable binding modes of flavonoids binding to the human aryl hydrocarbon receptor (3,6), compound inhibitor binding to C3c (4), compounds binding to the human COUP-TF1 and COUP-TF2 (5), as well as (*R*)-DHMA binding to *E. coli* Tsr (1), the latter of which is also investigated in the current study.

Here, we employed the in-house docking-refinement protocol (1) to determine the most energetically favorable binding mode of (*S*)-DHMA binding to pTsr. In line with the docking-refinement protocol and our previous study of (*R*)-DHMA binding to pTsr (1), the initial placement

of (*S*)-DHMA into the binding site of *E. coli* pTsr was guided by the experimentally resolved ligand serine bound in Chain A of the crystal structure of the serine:pTsr complex (PDB ID: 3ATP (7)) using the ShaEP algorithm (8), as previous experimental studies (9) showed that DHMA shares the same binding pocket as serine and that attractant chemotaxis to DHMA requires an intact serine-binding site in Tsr. Subsequently, short docking simulations were introduced to search binding modes of the (*S*)-DHMA:pTsr complex (Figure S1, cyan block). In the short docking simulations, 20 independent runs were performed, in which 200 steps of 2 ps simulations were conducted. For each of the 200 steps, the ligand was rotated about a randomly generated axis, followed by a 2 ps MD simulation and energetic minimization; data were saved for subsequent evaluation (Figure S1, cyan block). The result was 4000 saved binding modes of the (*S*)-DHMA:pTsr complex per docking simulation. Throughout the duration of the short docking simulations, (*S*)-DHMA was constrained in the binding site using quartic and harmonic spherical potentials through the MMFP module of CHARMM (10) (Figure S1, blue block). The binding pocket residues (56, 59-76, 81-94, 130-144, 147-162, 59'-76' – where residues marked with a prime symbol (') belong to the protein subunit of the pTsr dimer with fewer interacting residues (considered to be the minority side) were unconstrained and flexible. The absence of constraints on the binding pocket residues aimed to facilitate the ability of the residues to adopt to the different binding modes of the ligand generated through random rotations (Figure S1, yellow block, pocket encircled by red dotted lines). Five separate sets of docking simulations, or docking systems, were introduced to explore the possible binding modes of (*S*)-DHMA. Four docking systems utilized harmonic spherical potentials, and one system utilized a quartic spherical potential (Figure S1, orange blocks within blue block). The quartic spherical potential introduces an energetic well away from the center of the spherical potential and thus encourages the ligand to move away from its

initial position. The independent use of both quartic and harmonic spherical potentials allowed for the exploration of binding modes both away from (quartic) and in proximity to (harmonic) the initial positioning of the ligand (see Eq. 2 of ref. (1)). From each of the docking simulation systems, the three binding modes with the lowest interaction energy were selected for further investigation resulting in 15 binding modes (Figure S1, green and red blocks). The 15 binding modes of the (*S*)-DHMA:pTsr complex were investigated through 20 ns explicit-solvent MD simulations to refine the ligand:receptor structures, optimize intermolecular interactions, determine the structural stability of the selected binding modes, and determine the most energetically favorable binding modes. All MD simulations were performed in explicit solvent using CHARMM (10) and CHARMM36 topologies and parameters (11) with periodic boundary conditions. Topologies and parameters for (*S*)-DHMA were obtained from CGENFF (12). The energetic favorability of the binding modes was assessed using MM-GBSA association free-energy calculations (13), in line with our previous study on (*R*)-DHMA binding to pTsr (1). The predicted binding modes of (*S*)-DHMA with the most favorable average MM-GBSA association free-energy were compared with all other binding modes to ensure that all other binding modes were far less energetically favorable than the predicted mode. Binding modes with similar association free-energies to the predicted binding mode were visually inspected to verify that their structures were similar to the structure of the most energetically favorable binding mode (1). The structure resulting in the most energetically favorable binding mode was used as the initial structure of the (*S*)-DHMA:pTsr complex used for the subsequent five replicate 100 ns MD simulations described in the main text.

**Investigating (*R*)-DHMA and (*S*)-DHMA in complex with pTsr using multiple MD simulations.** From the 15 binding modes of (*R*)-DHMA:pTsr and the 15 binding modes of the (*S*)-DHMA:pTsr, we selected the most energetically favorable binding modes of (*R*)- and (*S*)-DHMA

in complex with pTsr for further investigation. Using the structures resulting in the most energetically favorable binding modes of (*R*)- and (*S*)-DHMA in complex with pTsr as initial structures, we performed five independent replicate 100 ns MD simulations of (*R*)- and (*S*)-DHMA in complex with pTsr with simulation snapshots extracted every 20 ps. Prior to the production run, the structures were equilibrated in two stages. In the first equilibration stage, the system was equilibrated using a 1 ns explicit solvent MD simulation, in which the heavy atoms of the ligand and Tsr backbone atoms were constrained with a harmonic force constant of 1.0 kcal/(mol·Å$^2$) and the Tsr side chain atoms were constrained with a harmonic force constant of 0.1 kcal/(mol·Å$^2$). In the second stage, all constraints on the Tsr protein were released and the ligand was lightly constrained with a harmonic force constant of 0.5 kcal/(mol·Å$^2$). Upon completion of the 100 ns MD simulations, we performed energetic and structural analyses on the 25,000 simulation snapshots resulting from the five replicate 100 ns MD simulations for each enantiomer.

To determine the presence of water-mediated interactions and their role in (*R*)- and (*S*)-DHMA binding, we developed FORTRAN programs to detect pTsr residues interacting with the enantiomers through water. A hydrogen bond donor/acceptor atom of a pTsr residue was considered to be interacting with (*R*)- or (*S*)-DHMA if (1) any of their hydrogen bond donor/acceptor atoms were within 3.5 Å of the oxygen of the same water molecule and (2) the angle between the vector from the oxygen of the water molecule to the atom of the given pTsr residue and the vector from the oxygen of the water molecule to the atom (*R*)- or (*S*)-DHMA was less than 150° (14).

To investigate and potentially differentiate the key interactions associated with the binding of (*R*)-DHMA and (*S*)-DHMA, we calculated the average interaction-free-energies between each pTsr residue and both ligands within their respective simulation snapshots using the MM-GBSA

approximation (13). The per-pTsr residue interaction-free-energies for each of the 5 replicate 100 ns MD simulation production run were calculated for their full duration, in increments of 200 ps, using CHARMM (10), Wordom (15), and in-house FORTRAN programs. The interaction-free-energies between the ligand and each pTsr residue were calculated using Eq. 1, as in refs. (1-5,16-18).

$$\Delta G_{RL}^{\text{inte}} = \sum_{i \in R} \sum_{j \in L} \left( E_{ij}^{\text{Elec}} + E_{ij}^{\text{GB}} \right) + \sum_{i \in R} \sum_{j \in L} E_{ij}^{\text{vdW}} + \gamma \sum_{i \in R,L} \Delta(\text{SASA}_i) \qquad \text{Eq. 1}$$

The polar component of the interaction-free-energy between a pTsr residue, *R*, and the ligand, *L*, is represented by the sum of the electrostatic, $E_{ij}^{\text{Elec}}$, and polar solvation, $E_{ij}^{\text{GB}}$, free-energy terms. The non-polar component of the interaction-free-energy between *R* and *L* is represented by the sum of the Van der Waals, $E_{ij}^{\text{vdW}}$, and non-polar solvation, $\gamma \cdot \text{SASA}$, free-energy terms.

The electrostatic interaction contribution represents the interaction between residue *R* and ligand *L*, and the polar solvation contribution represents the interaction of residue *R* with the solvent polarization potential induced by *L*. The van der Waals contribution represents the non-polar interaction between residue *R* and ligand *L*, and the non-polar solvation contribution represents the non-polar interactions with the surrounding solvent and cavity contributions due to binding. The solvation terms were determined using the GBSW generalized-Born model (19). The interaction free-energy-calculations were performed using a non-polar surface tension coefficient, $\gamma$, of 0.03 kcal/(mol$\text{Å}^2$) (20).

The per-residue interaction-free-energy between pTsr residues and the two ligands, (*R*)- and (*S*)-DHMA, were independently averaged over the number of simulation snapshots and number of replicate MD simulations (five MD simulations). The energetically favorable per-residue interaction-free-energy values between pTsr residues and the two ligands, defined as those with

energy values less than -1 kcal/mol, are decomposed into polar and non-polar contributions and are presented in Figure 2.

**Investigating serine bound and apo pTsr.** We performed five 100 ns MD simulations of serine in complex with pTsr and two 100 ns MD simulations of an unbound (apo) Tsr. The simulations were performed as controls to ensure that the observed piston-like push-down of α-helix 4 is not an artifact of the MD simulations and is observed in simulations of a known Tsr chemoattractant (serine) and not observed in the apo pTsr. The starting structure of the serine:Tsr complex corresponded to the crystal structure of pTsr bound by serine (PDB ID: 3ATP) (7) with the bound serine in Chain B removed. While Tsr contains two symmetric serine-binding sites, only one functional site suffices for serine sensing (21,22). Thus, for a fair comparison with the binding of (*R*)-DHMA and (*S*)-DHMA to pTsr, the second bound serine within the crystal structure with disordered electron density (7) was removed. The starting structure of the apo pTsr corresponded to the crystal structure of pTsr bound by serine (PDB ID: 3ATP) (7) with both bound serine ligands removed. The simulation setup and parameters were the same as those used to investigate the binding of (*R*)- and (*S*)-DHMA described above and in ref. (1). Upon completion of the 100 ns MD simulations, we calculated the projected lengths of α-helix 4 per simulation snapshot for each simulation run as described in *Investigating piston-like motions in pTsr caused by binding of (R)-DHMA and (S)-DHMA*. The projected lengths are shown in Figure S3.

**Data S1.** Coordinates of (*R*)- and (*S*)-DHMA in complex with pTsr from the 100-ns MD simulations provided in PDB format. The 25 ns, 50 ns, 75 ns, and 100 ns MD coordinates of the MD simulated (*R*)-DHMA:Tsr complex and the MD simulated (*S*)-DHMA:Tsr complex are provided as *Supporting Material* in PDB format. The structures are aligned with respect to the backbone of the entire modeled pTsr. The correspondence of PDB files and the number of the MD simulation from which the coordinates originate are shown in the table.

| PDB file | Complex | Simulation |
|---|---|---|
| coordinates.rdhma1.pdb | (*R*)-DHMA | 1 |
| coordinates.rdhma2.pdb | (*R*)-DHMA | 2 |
| coordinates.rdhma3.pdb | (*R*)-DHMA | 3 |
| coordinates.rdhma4.pdb | (*R*)-DHMA | 4 |
| coordinates.rdhma5.pdb | (*R*)-DHMA | 5 |
| coordinates.sdhma1.pdb | (*S*)-DHMA | 1 |
| coordinates.sdhma2.pdb | (*S*)-DHMA | 2 |
| coordinates.sdhma3.pdb | (*S*)-DHMA | 3 |
| coordinates.sdhma4.pdb | (*S*)-DHMA | 4 |
| coordinates.sdhma5.pdb | (*S*)-DHMA | 5 |

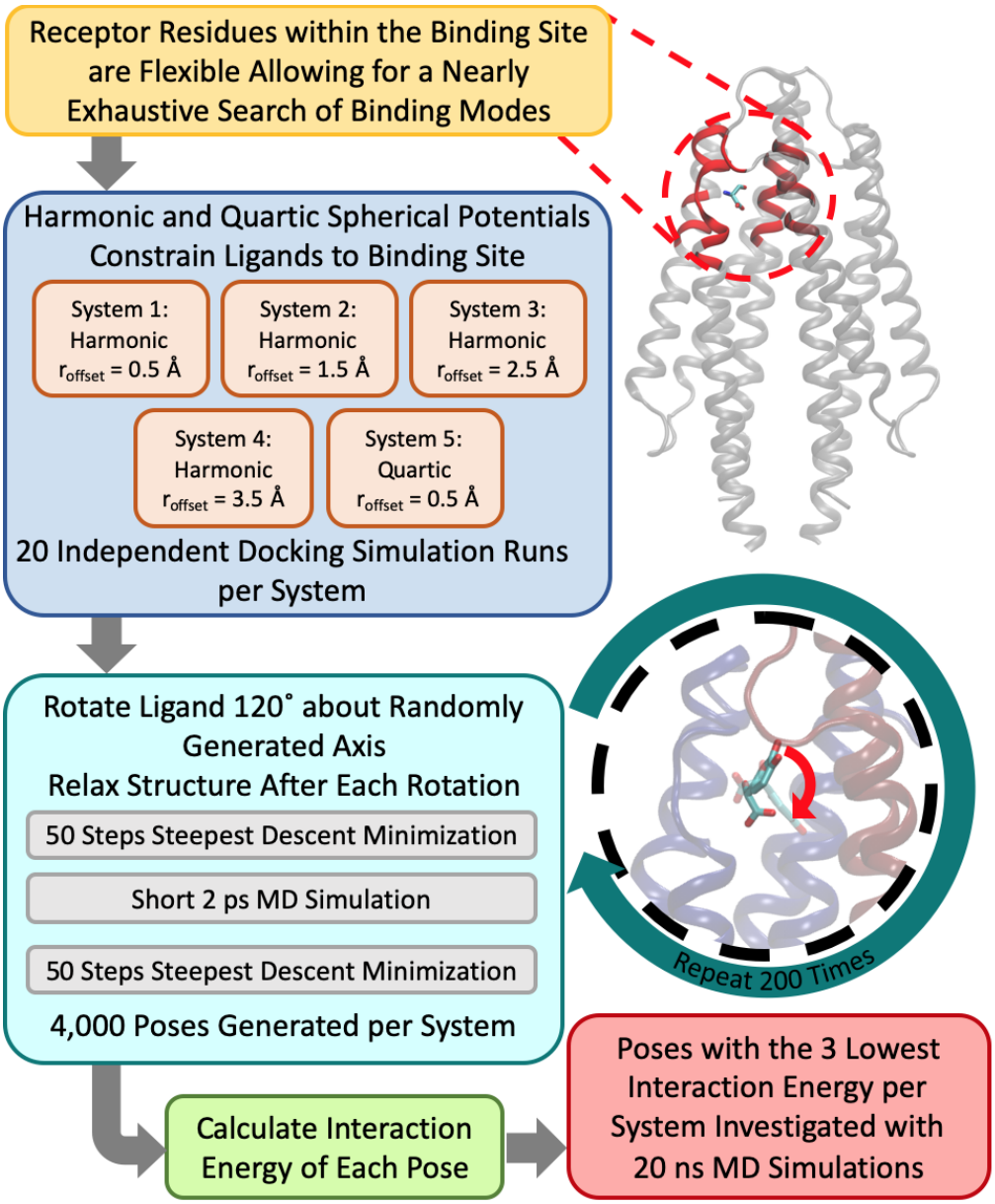


**Figure S1.** Workflow for the docking refinement protocol used to obtain the most energetically favorable binding mode of (*S*)-and (*R*)-DHMA in complex with pTsr, which were used as initial structures for the five replicate multi-ns MD simulations.

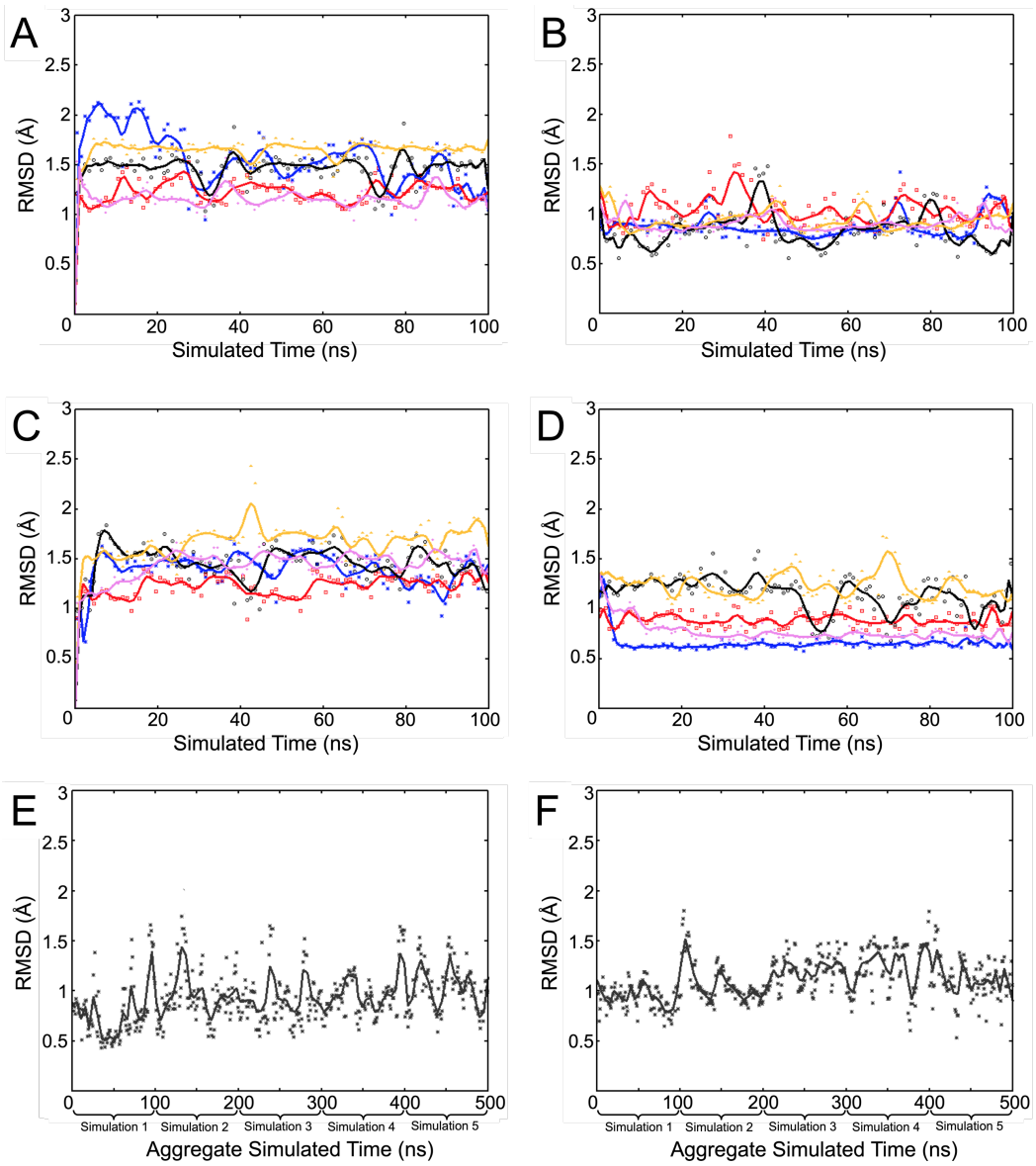


**Figure S2.** RMSD (in Å) of (A,B) (*R*)-DHMA and (C,D) (*S*)-DHMA with respect to (A,C) their respective initial structures and (B,D) their respective average structures throughout independent 100 ns simulations. RMSD (in Å) of (E) (*R*)-DHMA and (F) (*S*)-DHMA with respect to their respective average structures throughout their five combined 100 ns simulations. The plotted RMSD values correspond to values extracted every 1 ns. The plotted RMSD values correspond to values extracted every 1 ns. Solid lines correspond to Bezier curves fitted to RMSD values extracted every 0.1 ns. Blue, red, black, yellow, and pink data points and lines correspond to data extracted from the simulations starting from the first, second, third binding mode differing from the lowest association free-energy binding mode for each of the complexes.

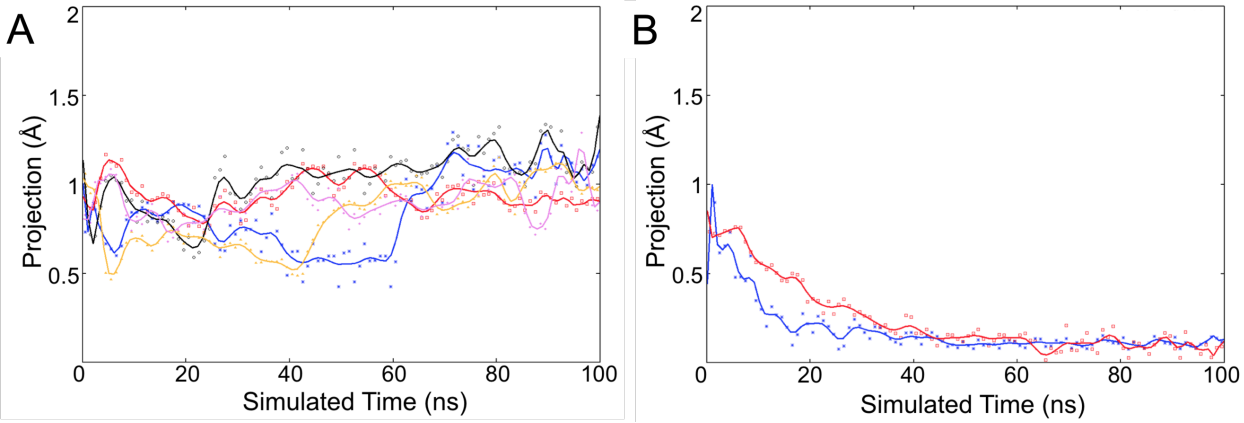


**Figure S3.** Vector projections showing the normalized magnitude of piston-like motions (in Å) within α-helix 4 of pTsr (A) bound to serine and (B) unbound with respect to the simulated time (in ns). The projection values plotted correspond to projected lengths, $p_i$, calculated using Eq. 2 and extracted every 1 ns. Solid lines correspond to Bezier curves fitted to projected lengths extracted every 0.1 ns. (A) Blue, red, black, yellow, and pink data points and lines correspond to data extracted from the first, second, third, fourth, and fifth simulations, respectively. (B) Blue and red data points and lines correspond to data extracted from the first and second simulations, respectively.

**Supporting experimental material**

**Resolution and isolation of DHMA enantiomers.** $^1$H NMR data were recorded at 25 °C using an INOVA-500 equipped with Prodigy Cold Probe NMR at 500 MHz. Chemical shifts are reported in ppm using the solvent resonance as the internal standard ($^1$H NMR $CD_3C(O)CD_3$:δ 2.05 ppm). Data are reported as follows: chemical shift, multiplicity (s = singlet, d = doublet, t = triplet, q = quartet, bs = broad singlet, m = multiplet, or any combination of these), coupling constants (Hz) and integration. Low Resolution Mass Spectrometry (LRMS) analysis was obtained using an Amazon ion-trap mass spectrometer utilizing Electrospray Ionization (ESI), and the data are reported as m/z (relative intensity). Optical rotations were recorded at 589 nm employing a 25 mm cell. Specific rotations $[\alpha]_D^{20}$, are reported in degree mL/(g•dm) at the specific temperature. HPLC separations were run using an Agilent 1200 series (analytical) or an Agilent 1260 Infinity system (preparative). Preparative reversed-phase HPLC was done using a Gemini 5 micron C18 110A (100 x 21.2 mm) AXIA column. Analytical chiral stationary phase HPLC separations were run on a CHIRALPAK ID-3 (150 x 4.6 mm I.D., 3 micron) column, and preparative chiral stationary phase HPLC separations were run on a CHIRALPAK ID (250 x 20 mm I.D., 5 micron) column. The Amano Lipase PS was purchased from Sigma Aldrich. THF and MTBE were used in the kinetic resolution without drying the solvents.

**Separation of (*R*)-DHMA and (*S*)-DHMA.** Analytical separation was achieved with a CHIRALPAK ID-3 (150 x 4.6 mm I.D., 3 micron) column using methanol/water (10:90) and 0.1% formic acid as the mobile phase (0.6 ml/min flow rate). On the analytical HPLC column, the enantiomers of DHMA had retention times of 4.0 and 5.9 min, and we assigned the (*R*) and (*S*) configuration, respectively (Figure S4).

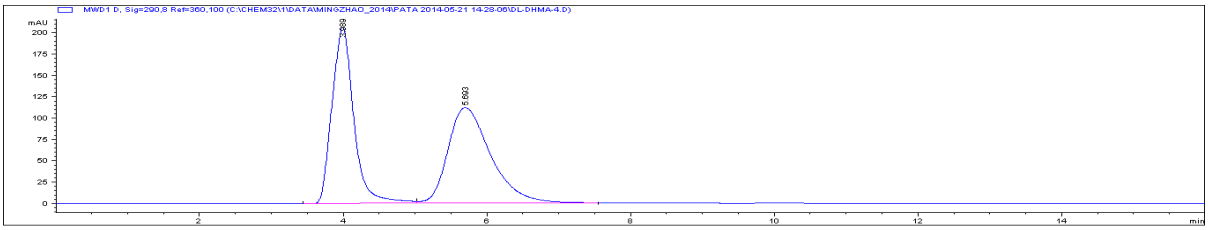


**Figure S4.** Chromatogram of racemic DHMA on the chiral analytical column (DHMA 3 mg/mL in MeOH, 4 µL injection).

Preparative separation was achieved with a CHIRALPAK ID (250 x 20 mm I.D., 5 micron) column using methanol/water (20:80) and 0.1% formic acid as the mobile phase (10 ml/min flow rate). On the preparative HPLC column, the enantiomers of DHMA had retention times of 6.9 and 8.3 min., and we assigned the (*R*) and (*S*) configuration, respectively (Figure S5).

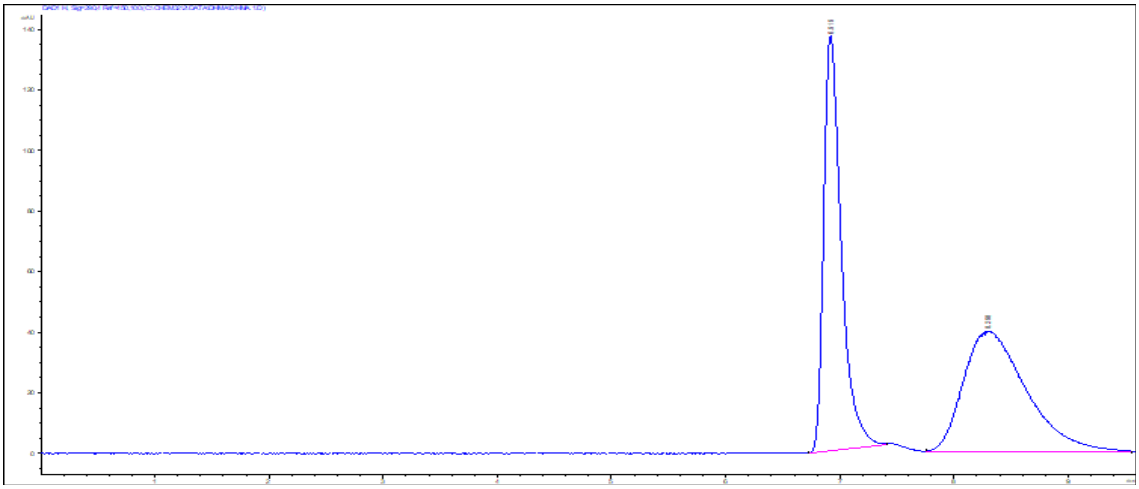

Signal 1: DAD1 H, Sig=290,4 Ref=450,100

| Peak # | RetTime [min] | Type | Width [min] | Area [mAU*s] | Area % |
|---|---|---|---|---|---|
| 1 | 6.919 | BB | 0.1381 | 1467.42883 | 49.3925 |
| 2 | 8.298 | BB | 0.4504 | 1503.52576 | 50.6075 |

**Figure S5.** Chromatogram of racemic DHMA on the chiral preparative column (DHMA 10 mg/mL in MeOH, 120 µL injection).

**(*R*)-DHMA and (*S*)-DHMA separated by preparative HPLC.** A solution of racemic DHMA (20 mg, 10 mg/mL) was separated as described above with 4 injections (~ 500 µL each) on the preparative column. The fractions containing each peak were combined, concentrated, then freeze-dried on a lyophilizer overnight to provide 9 mg of (*R*)-DHMA (RT = 6.9 min) and 8 mg of (*S*)-DHMA (RT = 8.3 min).

**(*R*)-DHMA** All spectral data for this compound were consistent with those previously reported for racemic DHMA (Sigma-Aldrich and BioRad), > 98% ee by HPLC analysis, Optical rotation [α] – 209.9 (*c* 0.465, MeOH) (Figure S6).

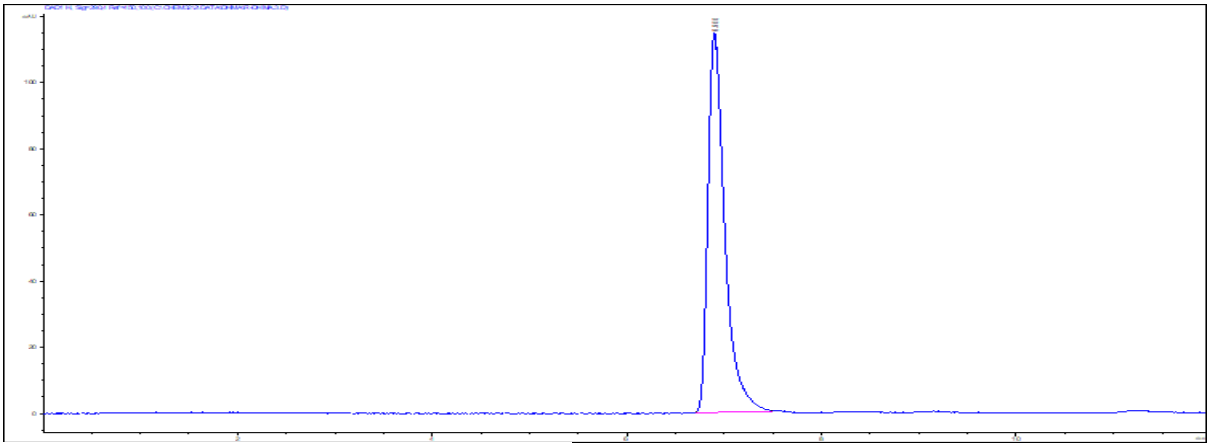

Signal 1: DAD1 H, Sig=290,4 Ref=450,100

| Peak # | RetTime [min] | Type | Width [min] | Area [mAU*s] | Area % |
|---|---|---|---|---|---|
| 1 | 6.900 | BB | 0.1513 | 1379.70410 | 100.0000 |
| Totals : | | | | 1379.70410 | |

**Figure S6.** Chromatogram of (*R*)-DHMA after separation by HPLC (chiral prep column, 5 mg/mL in MeOH, 150 µL injection).

**(*S*)-DHMA** All spectral data for this compound were consistent with those previously reported for racemic DHMA (Sigma-Aldrich and BioRad), 94% ee by HPLC analysis, optical rotation [α] + 195.2 (*c* 0.31, MeOH) (Figure S7).

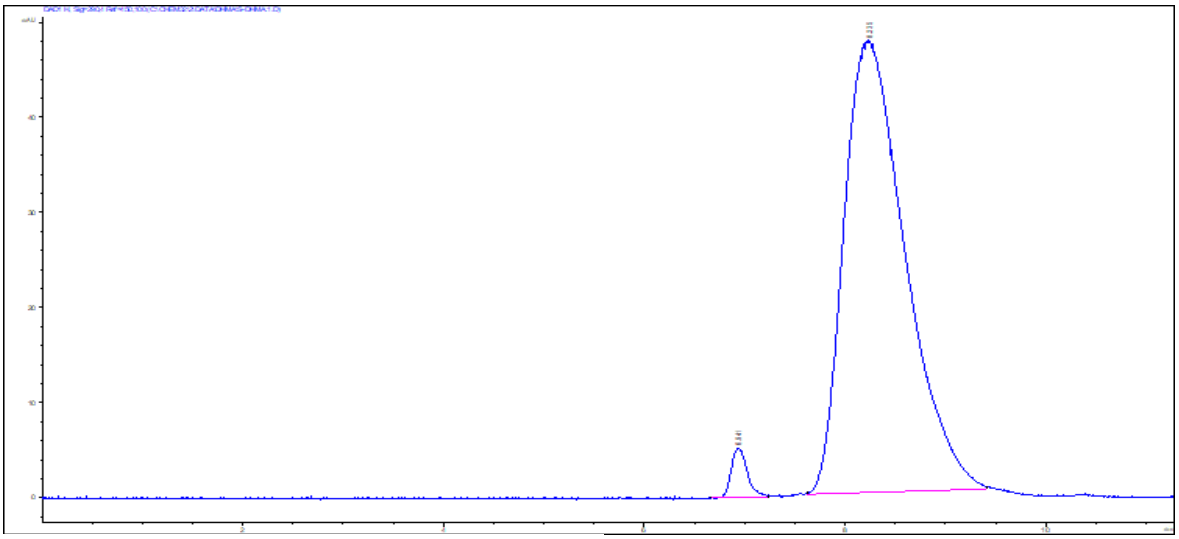

| Peak # | RetTime [min] | Type | Width [min] | Area [mAU*s] | Area % |
|---|---|---|---|---|---|
| 1 | 6.941 | BB | 0.1334 | 56.78226 | 2.7439 |
| 2 | 8.235 | BB | 0.4968 | 2012.60059 | 97.2561 |
| Totals : | | | | 2069.38285 | |

**Figure S7.** Chromatogram of (*S*)-DHMA after separation by HPLC (chiral prep column, 5 mg/mL in MeOH, 120 µL injection).

**Kinetic resolution of racemic DHMA, isolation of enriched (*R*)-DHMA 2 and acetate 3.** Amano Lipase PS (~ 5 mg) was added to a stirred solution of racemic DHMA (22 mg, 0.12 µmol, 1 equivalent) and vinyl acetate (300 mg, 3.49 mmol, 29 equiv) in methyl t-butyl ether/ THF (7:1, 2 ml). The resultant mixture was stirred at room temperature for 24 h. The reaction mixture was passed through a pad of celite, the pad was washed with 2 ml of THF, and the filtrate was concentrated. The crude mixture was purified by preparative reversed-phase HPLC using a Gemini 5 micron C18 110A (100 x 21.2 mm) AXIA column, gradient 5-95% $CH_3CN$/Water over 20 min.

Fractions containing each peak were freeze-dried on a lyophilizer overnight to yield unreacted (*R*)-DHMA **2** (RT = 5.1 min, 9 mg, 41% recovered yield) and acetate **3** (RT = 8.5 min., 10.3 mg, 40% yield) (Figure S8).

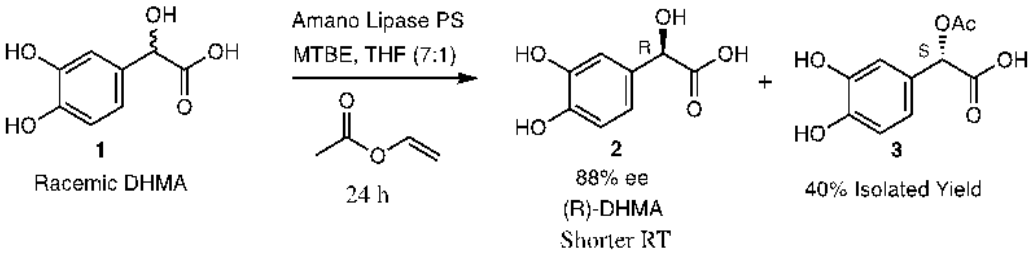


**Figure S8.** Reaction of racemic DHMA resulting in separated (*R*)-DHMA and reacted (*S*)-DHMA.

**Recovered (*R*)-DHMA** All spectral data for this compound was consistent with that previously reported for racemic DHMA (Sigma-Aldrich and BioRad), 88% ee by HPLC analysis (Figure S9).

**Acetate 3** $^{1}$H NMR (500 MHz, $CD_3COCD_3$) δ 6.97 (s, 1H), 6.90 - 6.72 (m, 2H), 5.68 (s, 1H), 2.08 (s, 3H); LRMS (ESI+) *m/z* calcd for $C_{10}H_9O_6$ $[M - H]^-$ : 183.0; found: 183.1 (Figure S10).

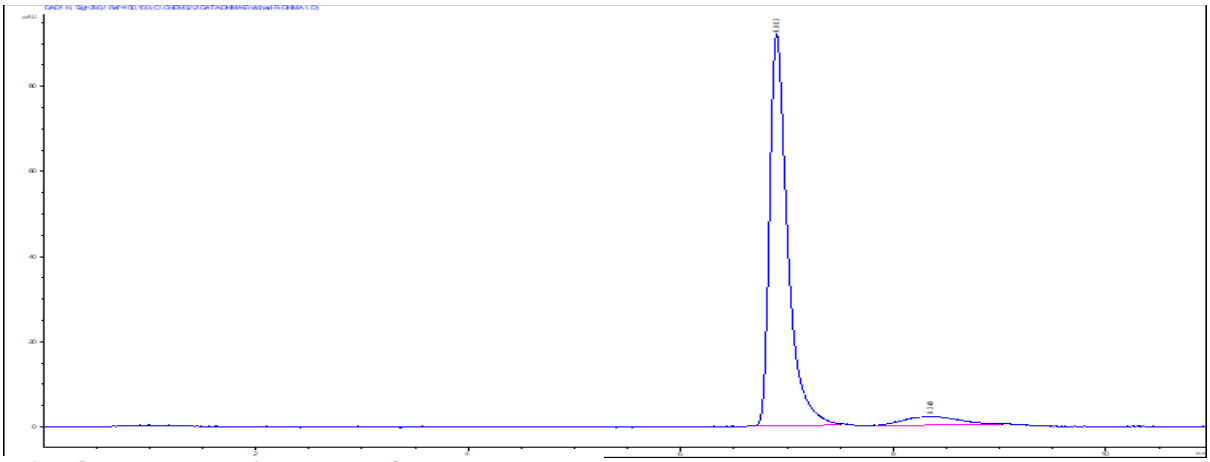

Signal 1: DAD1 H, Sig=290,4 Ref=450,100

| Peak # | RetTime [min] | Type | Width [min] | Area [mAU*s] | Area % |
|---|---|---|---|---|---|
| 1 | 6.903 | BB | 0.1635 | 1084.72852 | 93.7527 |
| 2 | 8.348 | BB | 0.4118 | 72.28207 | 6.2473 |
| Totals : | | | | 1157.01059 | |

**Figure S9.** Chromatogram of highly enriched (*R*)-DHMA isolated after kinetic resolution by HPLC (Chiral prep column, 2 mg/mL in MeOH, 200 µL injection).

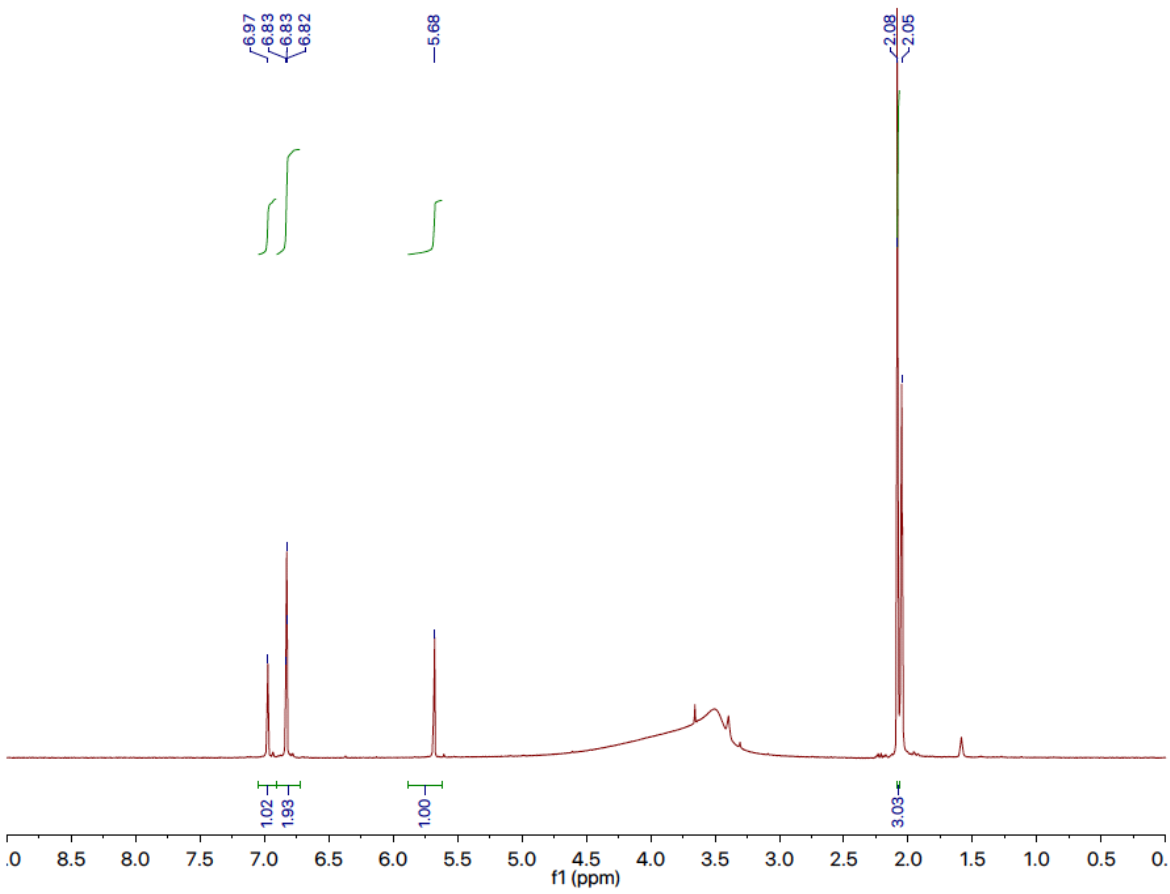


**Figure S10.** Acetate 3 $^{1}$H NMR (500 MHz, $CD_3COCD_3$). Acetate 3 $^{1}$H NMR (500 MHz, $CD_3COCD_3$) δ 6.97 (s, 1H), 6.90 - 6.72 (m, 2H), 5.68 (s, 1H), 2.08 (s, 3H).

**Supporting References**


(1) Orr, A. A., A. Jayaraman, and P. Tamamis. 2018. Molecular Modeling of Chemoreceptor: Ligand Interactions. Methods Mol. Biol. 1729:353-372.

(2) Jin, U. H., Y. Cheng, H. Park, L. A. Davidson, E. S. Callaway, R. S. Chapkin, A. Jayaraman, A. Asante, C. Allred, E. A. Weaver, S. Safe. 2017. Short chain fatty acids enhance aryl hydrocarbon (Ah) responsiveness in mouse colonocytes and Caco- 2 human colon cancer cells. Sci. Rep. 7(1):10163.

(3) Jin, U. H., H. Park, X. Li, L. A. Davidson, C. Allred, B. Patil, G. Jayaprakasha, A. A. Orr, L. Mao, R. S. Chapkin, A. Jayaraman, P. Tamamis, S. Safe. 2018. Structure-Dependent Modulation of Aryl Hydrocarbon Receptor-Mediated Activities by Flavonoids. Toxicol Sci. 164(1):205-217.

(4) Mohan, R. R., M. Wilson, R. D. Gorham Jr., R. E. S. Harrison, V. A. Morikis, C. A. Kieslich, A. A. Orr, A. V. Coley, P. Tamamis, D. Morikis. 2018. Virtual Screening of Chemical Compounds for Discovery of Complement C3 Ligands. A. C. S. Omega 3:6427–6438.

(5) Yoon, K., Chen, C. C., Liu, S., Orr, A. A., Barreto P. N., Tamamis, P., and Safe, S. 2019. Activation of COUP-TFI by a Novel Diindolymethane Derivative. Cells. 8(3): 220.

(6) Park, H., J. Un-Ho, A. A. Orr, S. P. Echegaray, L. A. Davidson, C. D. Allred, R. S. Chapkin, A. Jayaraman, K. Lee, P. Tamamis, and S. Safe. 2019. Isoflavones as Ah Receptor Agonists in Colon-Derived Cell Lines: Structure–Activity Relationships. Chem. Res. Toxicol. doi: 10.1021/acs.chemrestox.9b00352

(7) Tajima, H., K. Imada, M. Sakuma, F. Hattori, T. Nara, N. Kamo, M. Homma, and I. Kawagishi. 2011. Ligand specificity determined by differentially arranged common ligand-binding residues in bacterial amino acid chemoreceptors Tsr and Tar. J. Biol. Chem. 286(49):42200-42210.

(8) Vainio, M. J., J. S. Puranen, and M. S. Johnson. 2009. ShaEP: molecular overlay based on shape and electrostatic potential. J. Chem. Inf. Model. 49(2):492-502.

(9) Pasupuleti, S., N. Sule, W. B. Cohn, D. S. MacKenzie, A. Jayaraman, and M. D. Manson. 2014. Chemotaxis of *Escherichia coli* to norepinephrine (NE) requires conversion of NE to 3,4-dihydroxymandelic acid. J. Bacteriol. 196(23):3992-4000.

(10) Brooks, B. R., C. L. Brooks 3rd, A. D. Mackerell Jr., L. Nilsson, R. J. Petrella, B. Roux, Y. Won, G. Archontis, C. Bartels, S. Boresch, A. Caflisch, L. Caves, Q. Cui, A. R. Dinner, M. Feig, S. Fischer, J. Gao, M. Hodoscek, W. Im, K. Kuczera, T. Lazaridis, J. Ma, V. Ovchinnikov, E. Paci, R. W. Pastor, C. B. Post, J. Z. Pu, M. Schaefer, B. Tidor, R. M. Venable, H. L. Woodcock, X. Wu, W. Yang, D. M. York, and M. Karplus. 2009. CHARMM: the biomolecular simulation program. J. Comput. Chem. 30(10):1545-1614.

(11) Huang, J., and A. D. MacKerell Jr. 2013. CHARMM36 all-atom additive protein force field: validation based on comparison to NMR data. J Comput Chem. 34(25):2135-2145.

(12) Vanommeslaeghe, K., E. Hatcher, C. Acharya, S. Kundu, S. Zhong, J. Shim, E. Darian, O. Guvench, P. Lopes, I. Vorobyov, and A. D. Mackerell Jr. 2010. CHARMM general force field: A force field for drug-like molecules compatible with the CHARMM all-atom additive biological force fields. J Comput Chem. 31(4):671-690.

(13) Hayes, J. M., and G. Archontis. 2012. MM-GB(PB)SA Calculations of Protein-Ligand Binding Free Energies. Molecular Dynamics - Studies of Synthetic and Biological Macromolecules. L. Wang, editor. InTech, Southern Illinois University Carbondale, United States of America, pp. 171-190.

(14) Huggins, D. J., B. Tidor. 2011. Systematic placement of structural water molecules for improved scoring of protein-ligand interactions. Protein Eng Des Sel. (10):777-789.

(15) Seeber, M., A. Felline, F. Raimondi, S. Muff, R. Friedman, F. Rao, A. Caflisch, and F. Fanelli. 2011. Wordom: a use(R)-friendly program for the analysis of molecular structures, trajectories, and free energy surfaces. J. Comput. Chem. 32(6):1183-1194.
(16) Tamamis, P., C. A. Kieslich, G. V. Nikiforovich, T. M. Woodruff, D. Morikis, and G. Archontis. 2014. Insights into the mechanism of C5aR inhibition by PMX53 via implicit solvent molecular dynamics simulations and docking. BMC Biophys. 7:5.
(17) Orr, A. A., M. M. Wördehoff, W. Hoyer, and P. Tamamis. 2016. Uncovering the Binding and Specificity of β-Wrapins for Amyloid-β and α-Synuclein. J Phys Chem B. 120(50):12781-12794.
(18) Orr, A. A., H. Shaykhalishahi, E. A. Mirecka, S. V. R. Jonnalagadda, W. Hoyer, and P. Tamamis. 2018. Elucidating the multi-targeted anti-amyloid activity and enhanced islet amyloid polypeptide binding of β-wrapins. Comput. Chem. Eng. 116(4): 322-332.
(19) Im, W., M. S. Lee, and C. L. Brooks 3rd. 2003. Generalized Born Model with a Simple Smoothing Function. J. Comput. Chem. 24:1691-1702.
(20) Knight, J. L., and C. L. Brooks 3rd. 2011. Surveying implicit solvent models for estimating small molecule absolute hydration free energies. J Comput Chem. 32(13):2909-2923.
(21) Lin, L. N., J. Li, J. F. Brandts, R. M. Weis. 1994. The serine receptor of bacterial chemotaxis exhibits half-site saturation for serine binding. Biochemistry. 33(21):6564-6570.
(22) Iwama, T., I. Kawagishi, S. Gomi, M. Homma, Y. Imae. 1995. In vivo sulfhydryl modification of the ligand-binding site of Tsr, the Escherichia coli serine chemoreceptor. J. Bacteriol. 177(8):2218-2221.